
Ammonia mapping observations toward the Galactic massive star-forming region Sh 2-255 and Sh 2-257

Mikito KOHNO^{1*}, Toshihiro OMODAKA², Toshihiro HANDA^{2,3}, James O. CHIBUEZE^{4,5}, Takumi NAGAYAMA⁶, Ross A. BURNS⁷, Takeru MURASE², Ren MATSUSAKA², Makoto NAKANO⁸, Kazuyoshi SUNADA⁶, Rin I. YAMADA⁹ and John H. BIEGING¹⁰

¹Astronomy Section, Nagoya City Science Museum, 2-17-1 Sakae, Naka-ku, Nagoya, Aichi 460-0008, Japan

²Graduate School of Science and Engineering, Kagoshima University, 1-21-35 Korimoto, Kagoshima, Kagoshima 890-0065, Japan

³Amanogawa Galaxy Astronomy Research Center (AGARC), Kagoshima University, 1-21-35 Korimoto, Kagoshima, Kagoshima 890-0065, Japan

⁴Centre for Space Research, Potchefstroom campus, North-West University, Potchefstroom 2531, South Africa

⁵Department of Physics and Astronomy, Faculty of Physical Sciences, University of Nigeria, Carver Building, 1 University Road, Nsukka 410001, Nigeria

⁶Mizusawa VLBI Observatory, National Astronomical Observatory of Japan, Osawa 2-21-1, Mitaka-shi, Tokyo 181-8588, Japan

⁷National Astronomical Observatory of Japan (NAOJ), 2-21-1 Osawa, Mitaka, Tokyo 181-8588, Japan

⁸Faculty of Science and Technology, Oita University, 700 Dannoharu, Oita, Oita 870-1192, Japan

⁹Department of Physics, Graduate School of Science, Nagoya University, Furo-cho, Chikusa-ku, Nagoya, Aichi 464-8602, Japan

Abstract

We performed NH_3 (J, K) = (1, 1), (2, 2), and (3, 3) mapping observations toward the Galactic massive star-forming region Sh 2-255 and Sh 2-257 using the Nobeyama 45-m telescope as a part of the KAGONMA (KAgoshima Galactic Object survey with the Nobeyama 45-metre telescope by Mapping in Ammonia lines) project. NH_3 (1, 1) has an intensity peak at the cluster S255 N, is distributed over $3 \text{ pc} \times 2 \text{ pc}$ and is located between two H II regions. The kinetic temperature derived from the $\text{NH}_3(2, 2)/(1, 1)$ ratio was $\sim 35 \text{ K}$ near the massive cluster S255 IR. These clusters also show emission with a large line width of $\sim 3\text{--}4 \text{ km s}^{-1}$. Based on the reported data we suggest that NH_3 gas in these regions is affected by stellar feedback from embedded YSO clusters in S255 IR and S255 N. We also detected NH_3 (1, 1) emission in a region west of the main gas clump at the location of a concentration of Class II YSOs adjacent to the H II regions Sh 2-254. The presence of Class II YSOs implies $\sim 2 \text{ Myr}$ of star formation, younger than Sh 2-254 ($\sim 5 \text{ Myr}$), thus we suggest that star formation in the western region could be influenced by the older H II region Sh 2-254.

Key words: ISM: H II regions — ISM: clouds — ISM: molecules — stars: formation — ISM: individual objects (Sh 2-254, Sh 2-255, Sh 2-256, Sh 2-257, S255 IR, S255 N)

1 Introduction

Sh 2-255 (=S255) and Sh 2-257 (=S257) are optically bright H II regions first cataloged by Sharpless (1959). They are confirmed as sites of massive star formation belonging to the Gemini OB1 Molecular Cloud Complex (e.g., Kawamura et al. 1998; Carpenter et al. 1995a; Carpenter et al. 1995b; Wang et al. 2017). Sh 2-254 (=S254) is an older (5.1 Myr) H II region, while Sh 2-256 (=S256) is a younger (0.2 Myr) H II region, both spatially located close to Sh 2-257 (Chavarría et al. 2008). This wider region, including multiple H II regions, is also called the Sh 254-258 (=S254-S258) complex. These regions have been studied in the optical, infrared, and radio wavelengths for over 4 decades. (e.g., Chopinet et al. 1974; Pipher & Soifer 1976; Evans et al. 1977; Mizuno 1982; Nakano et al. 1983; Heyer et al. 1989; Chavarría et al. 2008; Chavarría et al. 2014; Samal et al. 2015; Lim et al.

Table 1. Basic parameters of H II regions and embedded clusters

Name	l	b	$\log N_{\text{Ly}\alpha}$	Exciting Star	Age	References
	[$^{\circ}$]	[$^{\circ}$]	[photon s^{-1}]			
(1)	(2)	(3)	(4)	(5)	(6)	(7)
Sh 2-254	192.517	-0.146	47.71	O9.6 V	5.1 Myr	[1,3]
Sh 2-255	192.630	-0.018	47.92	O9.5-B0.0 V	1.5 Myr	[1,2, 3]
Sh 2-256	192.603	-0.129	46.86	B0.9 V	0.2 Myr	[1,3]
Sh 2-257	192.584	-0.083	47.51	B0.5	1.6 Myr	[1, 2, 3]
S255 IR	192.600	-0.049	45.11*	B1*	$7 \times 10^3 \text{ yr}^{\dagger}$	[2, 4]
S255 N	192.580	-0.040	45.55	B1	$2 \times 10^3 \text{ yr}^{\dagger}$	[2, 4]

The coordinates of 4 H II regions indicate the positions of an exciting star (Chavarría et al. 2008).

\dagger Dynamical time scale of outflows. * The value is adopted of the compact H II region S255-2a.

Columns: (1) Name (2) Galactic Longitude (3) Galactic Latitude (4) Number of the Lyman photon (5) Spectral type of the ionizing star (6) Age of the H II region and embedded cluster (7) References: [1] Chavarría et al. (2008), [2] Ojha et al. (2011), [3] Bieging et al. (2009), [4] Wang et al. (2011)

2015; Buslaeva et al. 2021; Ladeyschikov et al. 2021).

S255 IR (=S255-2) and S255 N are located between two H II regions and house young embedded clusters associated with maser sources (Wang et al. 2011). We summarized the properties of these H II regions and embedded clusters in Table 1. Previous studies suggest that the Sh 254–258 complex, including its H II regions, are at a common distance of ~ 2.0 kpc (e.g., Carpenter et al. 1995b). In this paper we adopt a distance of $1.78^{+0.12}_{-0.11}$ kpc obtained by annual parallax measurements of the H₂O maser source S255IR-SMA1 (Burns et al. 2016), noting that this value is consistent with the 1.786 kpc distance estimate for Gem OB1 reported in the Gaia DR2 (see Table 1 in Zucker et al. 2019). Figures 1 (a) and (b) present the Digital Sky Survey (DSS) optical image and ¹²CO $J = 2-1$ integrated intensity map, respectively, and in which the yellow boxed zone indicates the NH₃ mapping area. Sh 2-255 and Sh 2-257 are bright in the optical image, and in their intermediate region exists a dark lane which is seen to obscure the edge of Sh 2-257.

The ¹²CO emission has a peak at the location of S255 IR, which is a massive star-forming region (Burns et al. 2016; Hirota et al. 2021; Liu et al. 2020) associated with 6.7 GHz methanol masers (Rygl et al. 2010) and embedded massive YSOs seen as the three infrared sources of IRS-1 (=NIRS-3), IRS-2, and IRS-3 (e.g., Howard et al. 1997; Miralles et al. 1997; Itoh et al. 2001; Zinchenko et al. 2015; Zinchenko et al. 2012; Liu et al. 2018; Zinchenko et al. 2020; Uchiyama et al. 2020). S255 NIRS-3 was the first reported case of an accretion burst in a massive protostar (e.g., Fujisawa et al. 2015; Caratti o Garatti et al. 2017; Cesaroni et al. 2018; Szymczak et al. 2018). S255 N, located to the north between the two H II regions, also shows signs of active star formation and possibly hosts a

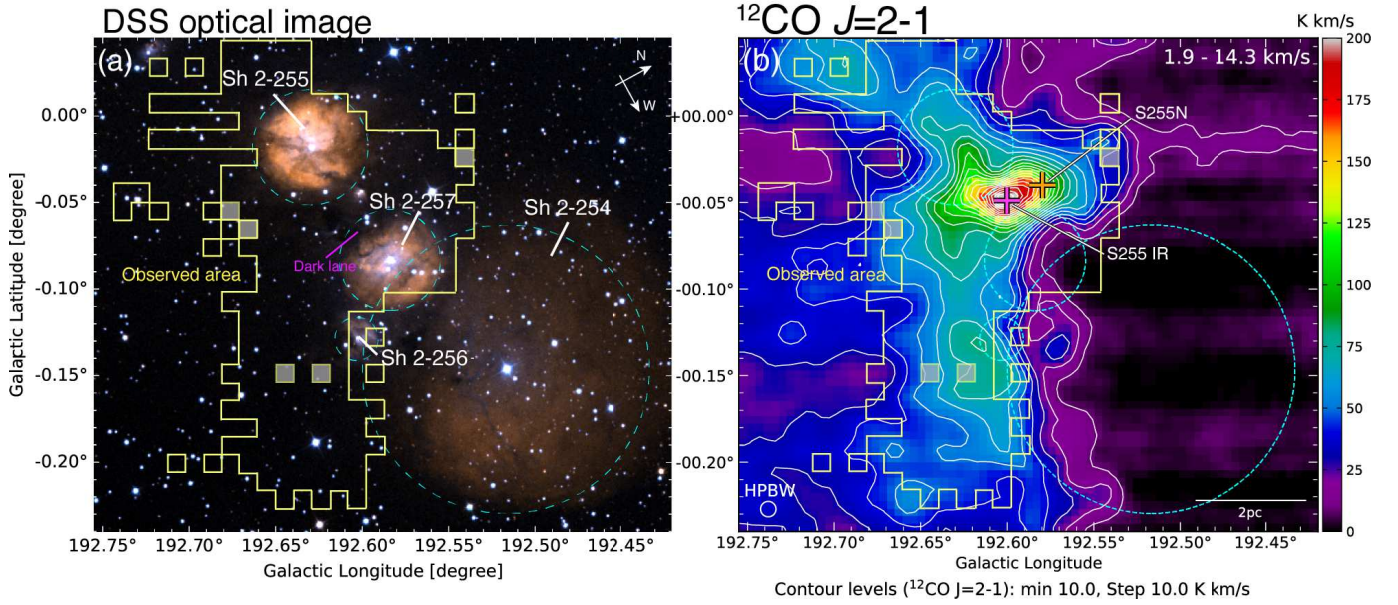


Fig. 1. (a) Three color composite image of Sh 2-255 and Sh 2-257. Blue, green, and red show DSS2 blue, (DSS2 blue + DSS2 red)/2, and DSS2 red, respectively. (b) $^{12}\text{CO } J=2-1$ integrated intensity map obtained by Bieging et al. (2009). Purple and yellow cross indicates the position of the embedded cluster S255 IR and S255 N, respectively. The yellow boxes show the NH₃ mapping area of our observation. Blue dotted circles enclose the H II regions. The size of H II regions are obtained from Mizuno (1982) and Chavarría et al. (2008).

massive proto-cluster (Cyganowski et al. 2007; Zemlyanukha et al. 2018).

Recently, high-resolution (~ 0.1 pc scale) observations of dense cores in giant molecular clouds were carried out using radio interferometers (e.g., Billington et al. 2019), whereas large-scale NH₃ mapping observations (~ 10 pc scale) aiming to investigate the impact of stellar feedback and interactions in high-mass star formation remain limited. Sh 2-255 and Sh 2-257 are ideal for studying the interaction between H II regions and molecular clouds. Therefore, we have carried out NH₃ mapping observations toward the Sh 2-255 and Sh 2-257 regions to reveal the dense gas and star-forming mechanism in the giant molecular cloud.

The paper is structured as follows: section 2 introduces observations and archive data sets; section 3 presents the NH₃ results; in section 4, we discuss possible star formation scenarios in the Sh 2-255 and Sh 2-257 region, and in section 5 we present a summary of this work.

2 Observations

2.1 NH₃ mapping observations using the Nobeyama 45 m telescope.

Our observations were carried out as a part of an NH₃ survey lead by Kagoshima University using the Kagoshima 6-m (Omodaka et al. 1994), Kashima 34-m, and Nobeyama 45-m telescopes (Galactic Centre: Nagayama et al. 2007; Nagayama et al. 2009, NGC 7000: Toujima et al. 2011, Monkey Head

Table 2. Observational properties of data sets.

Telescope	Line	Rest freq. [GHz]	Receiver	HPBW	Velocity Resolution	RMS noise level	References
(1)	(2)	(3)	(4)	(5)	(6)	(7)	(8)
Nobeyama 45-m	$\text{NH}_3(J, K) = (1, 1)$	23.694	H22	75''	0.39 km s ⁻¹	~ 0.02 K	This work
	$\text{NH}_3(J, K) = (2, 2)$	23.723	H22	75''	0.39 km s ⁻¹	~ 0.02 K	This work
	$\text{NH}_3(J, K) = (3, 3)$	23.870	H22	75''	0.39 km s ⁻¹	~ 0.02 K	This work
HHT 10-m	$^{12}\text{CO } J = 2-1$	230.538		32''	1.3 km s ⁻¹	~ 0.50 K	Bieging et al. (2009)

Columns: (1) Telescope name (2) Molecular lines (3) Rest frequency (4) Receiver (5) Half-power beam width (6) Velocity resolution (7) r.m.s noise level (8)

References

Nebula: Chibueze et al. 2013, AFGL 333-Ridge: Nakano et al. 2017, Sh 2-235: Burns et al. 2019, W33: Murase et al. 2020; Murase et al. 2022, Canis Major OB1: Hirata et al. 2021).

Mapping observations of $\text{NH}_3(J, K) = (1, 1), (2, 2), (3, 3)$, where J and K denote the quantum number of the total angular momentum and projected angular momentum along the molecular axis, respectively (Ho & Townes 1983), were carried out toward the Sh 2-255 and Sh 2-257 massive star-forming region using the Nobeyama 45-m telescope from December 2013 to June 2014, and December 2014 to June 2015 as part of a backup observation program (PI T. Omodaka BU135001 and BU145001). The rest frequency of $\text{NH}_3(1,1)$, $(2,2)$, and $(3,3)$ are 23.694 GHz, 23.723 GHz, and 23.870 GHz, respectively.

Data were acquired using multi-ON-OFF switching observations (three ON points for every one OFF position) toward the Sh 2-255 and Sh 2-257 region adopting a map center position of $(l, b) = (192^\circ 6285, -0^\circ 0548)$. Telescope pointing was adjusted to remain within an accuracy of 5'' using hourly cross-pattern scans of the H_2O maser source S235 ($\alpha_{\text{J2000}}, \delta_{\text{J2000}} = (05^{\text{h}}40^{\text{m}}51.^{\text{s}}96, +35^{\text{d}}41'47.''0)$). The system noise temperature (T_{sys}) during observations varied in the range of 120–200 K. The primary beam half-power beam width (HPBW) and the map grid spacing were 75'' and 37.''5, respectively. For the system front-end we used the H22 High Electron Mobility Transistor (HEMT) receiver in dual-polarization mode and for the back-end we utilized the digital spectrometer of Spectral Analysis Machine of the 45 m telescope (SAM45:Kuno et al. 2011; Kamazaki et al. 2012). Eight Intermediate Frequencies (IF) channels were used to record data for the three NH_3 lines and H_2O maser simultaneously in dual polarizations. The frequency bandwidth and spectral resolution in each IF were 125 MHz and 30.52 kHz, respectively, corresponding to 1600 km s⁻¹ and 0.39 km s⁻¹ velocity coverage and velocity spacing at 23 GHz.

Data were processed using the NEWSTAR¹ software package (Ikeda et al. 2001). We also

¹ <https://www.nro.nao.ac.jp/~nro45mrt/html/obs/newstar/index.html>

performed Hanning smoothing (width=5) in the frequency domain to improve the signal-to-noise ratio of detected emission. This paper describes the NH_3 emission in units of antenna temperature (T_a^*) calibrated using the chopper wheel method (Ulich, & Haas 1976; Kutner, & Ulich 1981). The root-mean-square noise level for the fully processed data cube after summing the two polarisations was ~ 0.02 K.

2.2 Archival data

We also make use of ^{12}CO $J=2-1$ data obtained by the Heinrich Hertz Submillimeter Telescope (HHT: Bieging et al. 2009). We converted the available data cube from the T_a^* scale divided by the main beam efficiency ($\eta_{\text{mb}} = 0.75$) to units of main beam temperature (T_{mb}). The HPBW and velocity resolution were $32''$ and 1.3 km s^{-1} , respectively. Detailed information regarding the CO observations is presented in Bieging et al. (2009), and the basic properties of the NH_3 and CO observations are summarized in Table 2.

We obtained optical and infrared images from the SkyView web page (McGlynn et al. 1998)². These data are taken from the Digitized Sky Surveys 2 (DSS2) and the Wide-field Infrared Survey Explorer, WISE telescope (Wright et al. 2010), respectively. In addition, we utilize a YSO catalog, including Class I and Class II protostellar objects identified by Chavarría et al. (2008).

3 Results

3.1 NH_3 spatial distributions

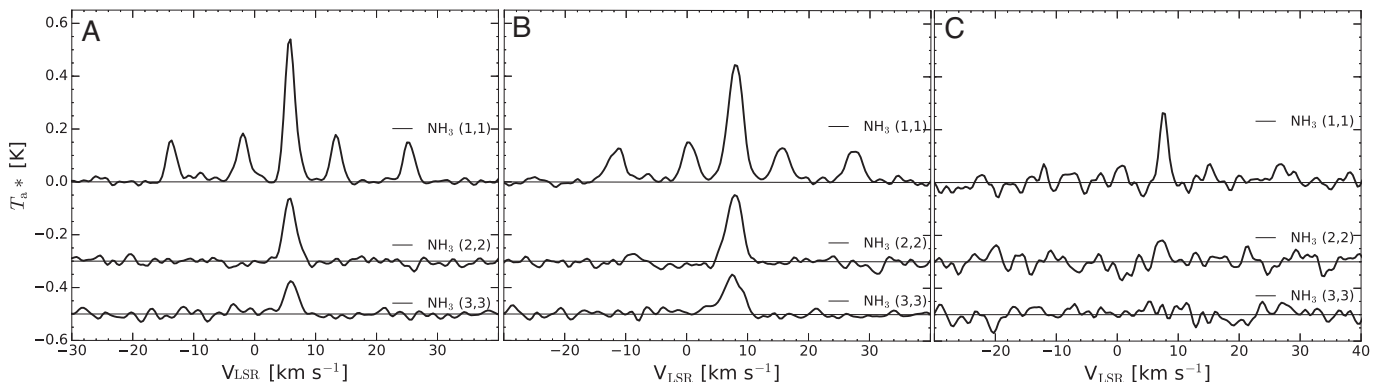


Fig. 2. NH_3 spectra at A $(l, b) = (192^\circ 613, -0^\circ 045)$, B $(l, b) = (192^\circ 572, -0^\circ 045)$, and C $(l, b) = (192^\circ 634, -0^\circ 159)$. These positions are also presented in Figure 3(a)

Figure 2 (a), (b), and (c) shows the NH_3 $(J, K) = (1, 1), (2, 2),$ and $(3, 3)$ spectra at map positions

² <https://skyview.gsfc.nasa.gov/current/cgi/titlepage.pl>

Table 3. Typical NH₃ spectra parameters of the main line

Position	l	b	Transition	T_a^*	v_{LSR}	Δv
	[degree]	[degree]	(J, K)	[K]	[km s ⁻¹]	[km s ⁻¹]
(1)	(2)	(3)	(4)	(5)	(6)	(7)
A	192.613	-0.045	(1,1)	0.53	5.8	2.1
			(2,2)	0.24	5.8	2.4
			(3,3)	0.13	6.0	2.5
B	192.572	-0.045	(1,1)	0.45	8.0	3.0
			(2,2)	0.26	7.8	2.9
			(3,3)	0.14	7.5	3.9
C	192.634	-0.159	(1,1)	0.27	7.6	1.6
			(2,2)	0.09	7.3	1.8
			(3,3)	—	—	—

Columns: (1) Spectra position (2) Galactic Longitude (3) Galactic Latitude (4) Rotational transition (5) Peak antenna temperature (6) Peak velocity by a single Gaussian fitting (7) The FWHM ($2\sigma\sqrt{2\ln 2}$) of spectra by a single Gaussian fitting, where σ is the standard deviation of the line profile.

A, B, and C, which signify the locations of S255 IR, S255 N, and a notable western gas clump, respectively. The map locations of these positions are indicated in Figure 3 (a). We detected the inner ($F_1 = 2 \rightarrow 1, 1 \rightarrow 2$) and outer satellite lines ($F_1 = 0 \rightarrow 1, 1 \rightarrow 0$) of the NH₃ (1,1) hyper-fine structure in spectra at positions A and B, where F_1 is the quantum number of the total angular momentum including nitrogen spin. We summarized the properties of each spectrum, obtained by a Gaussian fitting to the spectral data, in Table 3.

Figure 3 (a), (b), and (c) show the integrated intensity maps of NH₃ (1,1), (2,2), and (3,3), respectively. The lowest contours represent the detection threshold of $\sim 3\sigma$. NH₃ (1,1) has a peak at $(l, b) \sim (192^\circ 58, -0^\circ 045)$ and is distributed over $3 \text{ pc} \times 2 \text{ pc}$ ($l \times b$), elongated in the north-south direction. This peak is spatially consistent with the embedded cluster S255 N. On the other hand, NH₃ (2,2) and (3,3) emission is seen to peak at $(l, b) \sim (192^\circ 59, -0^\circ 045)$ and exhibit more compact distributions than NH₃(1,1). The NH₃ clump, including these peaks, exists between two H II regions Sh 2-255 and Sh 2-257. Hereafter, we call this dense gas as the ‘‘NH₃ dense clump’’. NH₃ spatial distributions are consistent with a previous study presented by Zinchenko et al. (1997). In addition, we also find a weak NH₃ (1,1) peak of the west of the NH₃ dense clump, at $(l, b) \sim (192^\circ 63, -0^\circ 16)$.

Figure 4 presents the NH₃ (1,1) velocity channel maps. NH₃ emission in the dense clump corresponding to S255 IR has a central velocity of $\sim 6 \text{ km s}^{-1}$. The northern intensity peak has a velocity range of 8-10 km s^{-1} , which is red-shifted from the center velocity of the NH₃ dense clump. The weak western emission has a velocity range of 7-8 km s^{-1} . Figure 5 (a) and (b) show the peak

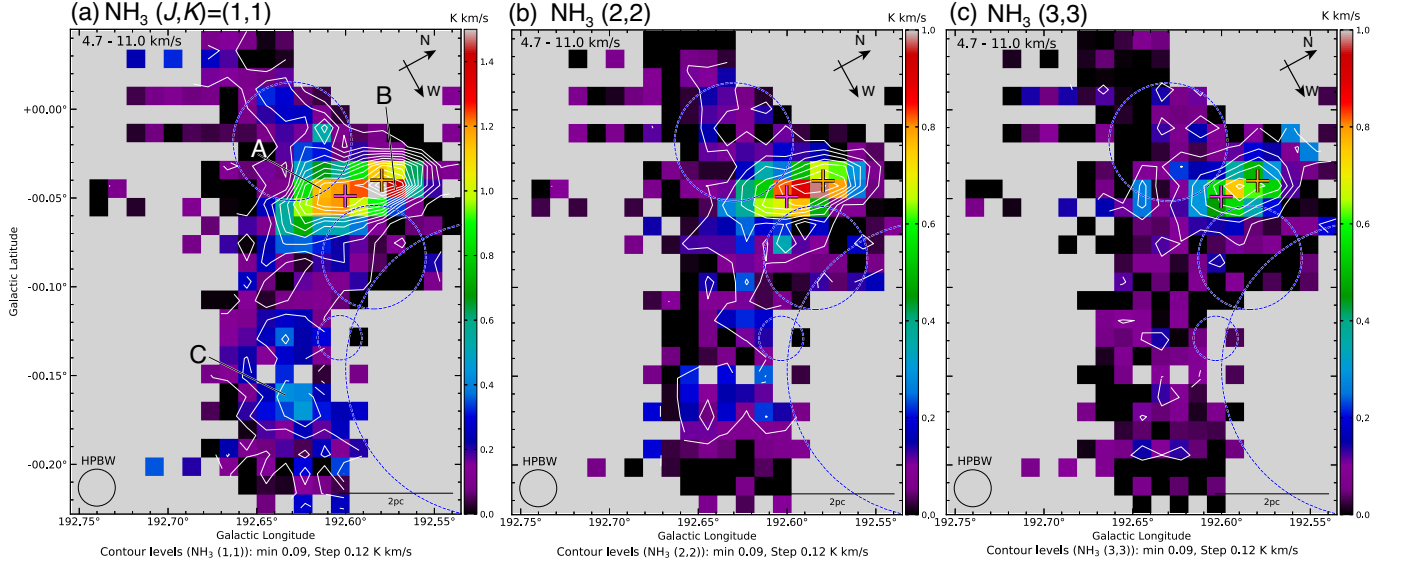


Fig. 3. Integrated intensity map of (a) NH_3 (1,1), (b) NH_3 (2,2), and (c) NH_3 (3,3). The lowest contour level and intervals are 0.09 K km s^{-1} ($\sim 3\sigma$) and 0.12 K km s^{-1} ($\sim 4\sigma$), respectively. A, B, and C represent the positions of the spectra in Figure 2. The purple, yellow crosses, and blue dotted circles are also the same as Figure 1(b).

velocity and emission line width maps, respectively, in which we derive line intensities and line widths from the height and full width half maximum (FWHM) of a Gaussian fit to the spectral profile at each map position.

We observed a velocity gradient spanning a range of $5.5\text{--}8.5 \text{ km s}^{-1}$ along the direction connecting the northern and southern regions of the NH_3 dense clump (Figure 5a), which corroborates previous results obtained for $^{12}\text{CO } J=3\text{--}2$ gas by Bieging et al. (2009) (see their Figure 7, left panel). The line width is widest towards the northern region near S255 IR and S255 N with a width of $\sim 3\text{--}4 \text{ km s}^{-1}$, but narrower towards the southern region with a width of $\sim 2 \text{ km s}^{-1}$. The western peak also has a narrow line width of $\sim 1\text{--}1.5 \text{ km s}^{-1}$ (Figure 5b).

3.2 Physical parameters of the NH_3 dense clump

We derived estimates of the optical depth, rotational temperature, and total column density using the methods presented by Ho & Townes (1983), Mangum et al. (1992), and Mangum & Shirley (2015). The optical depth can be derived from the ratio of the main and satellite line intensities. The optical depth $\tau(1, 1, m)$ of the NH_3 (1,1) main line is given by:

$$\frac{T_a^*(\text{main})}{T_a^*(\text{sate})} = \frac{1 - e^{-\tau(1,1,m)}}{1 - e^{-a\tau(1,1,m)}} \quad (1)$$

where T_a^* is the antenna temperature, and a is the theoretical intensity ratio of the main to the satellite line, which is $a = 0.278$ for the main to inner-satellite line ratio, and $a = 0.222$ of the main to outer-

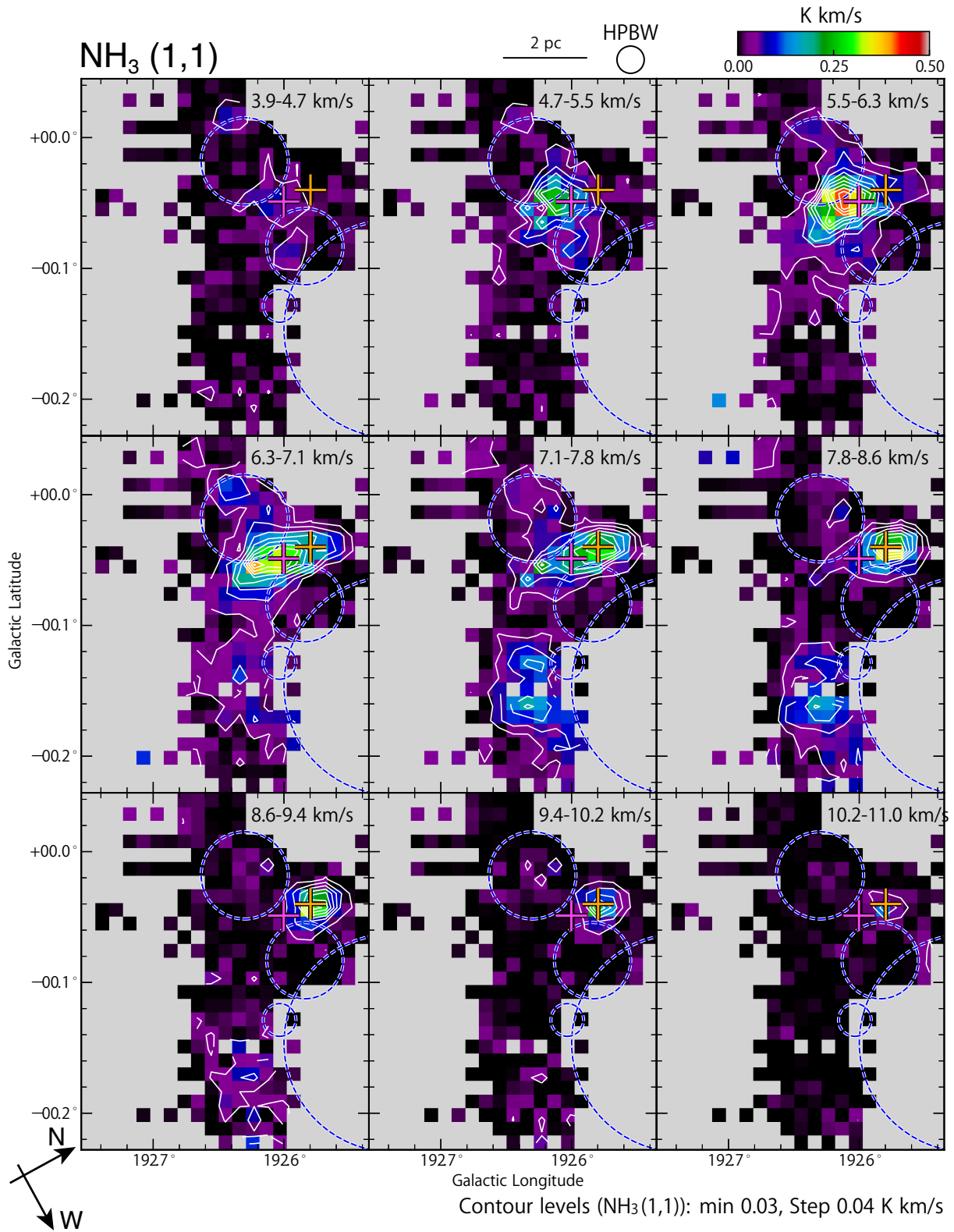


Fig. 4. Velocity channel map of $\text{NH}_3(1,1)$. The lowest contour level and intervals are 0.03 K km s^{-1} ($\sim 3\sigma$) and 0.04 K km s^{-1} ($\sim 4\sigma$), respectively. The purple, yellow crosses, and blue dotted circles are also the same as Figure 1(b).

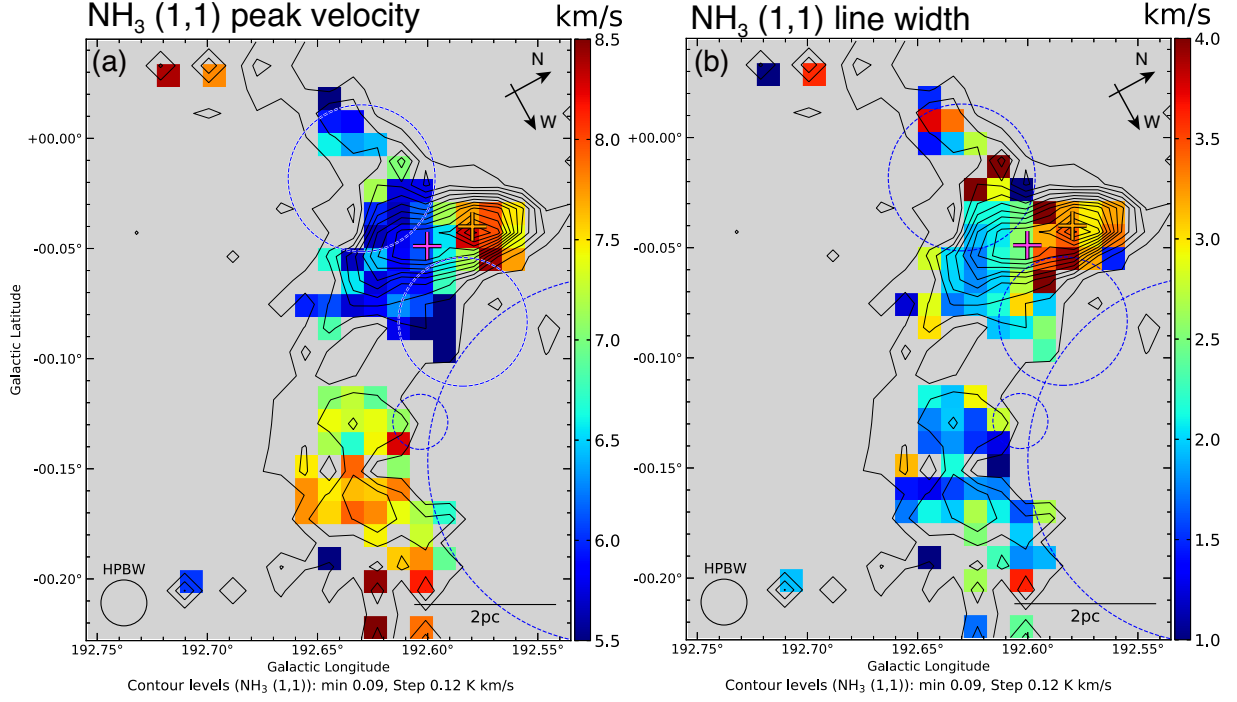


Fig. 5. (a) Peak velocity and (b) line width maps of NH_3 (J, K) = (1, 1) by fitting of the Gaussian function adopted of pixels above 0.08 K ($> 4\sigma$). The contours show the NH_3 (J, K) = (1, 1) integrated intensity. The purple, yellow crosses, and blue dotted circles are also the same as Figure 1 (b).

satellite line ratio (McGary & Ho 2002). In this paper averaged values of each pair of inner and outer satellite lines were used when deriving ratios to the main line intensity. To estimate physical parameters we adopted a mean value of optical depth for all map points where emission detections could be made above the 2σ noise level.

Assuming the same $\text{NH}_3(1,1)$ and $\text{NH}_3(2,2)$ line widths (Urquhart et al. 2011; Wienen et al. 2018), the rotational temperature can be derived from the main line intensities of NH_3 (1,1) and NH_3 (2,2) by the following equation (Ho & Townes 1983) :

$$T_{\text{rot}}(2,2 : 1,1) = -41.1 / \ln \left[\left(\frac{-0.282}{\tau(1,1,m)} \right) \times \ln \left\{ 1 - \frac{T_a^*(2,2,m)}{T_a^*(1,1,m)} \times (1 - e^{-\tau(1,1,m)}) \right\} \right] \text{ [K]}. \quad (2)$$

Figure 6(a) shows the rotational temperature distribution of NH_3 in the mapped region. The center of the NH_3 dense clump near S255 IR has a high rotational temperature of ~ 25 K, while the southern region has a comparatively lower rotational temperature of ~ 16 K. These values correspond to gas kinetic temperatures of (T_{kin}) ~ 35 K and ~ 18 K, respectively, using a conversion formula from Monte Carlo models (see Appendix B of Tafalla et al. 2004):

$$T_{\text{kin}} = T_{\text{rot}} / \left\{ 1 - \frac{T_{\text{rot}}}{41.1} \ln \left[1 + 1.1 \exp \left(-\frac{16}{T_{\text{rot}}} \right) \right] \right\} \text{ [K]} \quad (3)$$

The peak gas kinetic temperature is consistent with $T_{\text{kin}} = 35$ K obtained by the $\text{CH}_3\text{C}_2\text{H}$ $J = 6-5$ data (see Table 8 in Zinchenko et al. 2009). We note that the rotational temperature peak is located near S255 IR but does not coincide with it completely (Figure 6a). The measurement uncertainties might explain this displacement because it is smaller than the HPBW of our observations.

Using a prescription from Mangum et al. (1992), the NH_3 (1,1) column density assuming Local Thermal Equilibrium (LTE) is given by:

$$N(1,1) = 2.78 \times 10^{13} \tau(1,1,m) \left(\frac{T_{\text{rot}}}{[\text{K}]} \right) \left(\frac{\Delta v}{[\text{km s}^{-1}]} \right) [\text{cm}^{-2}] \quad (4)$$

where Δv is the line width of the NH_3 (1,1) main line (Figure 5b).

In addition, we estimated the NH_3 total column density of all energy levels using $N(1,1)$ (Turner 1991; Wilson et al. 2013; Mangum & Shirley 2015). The total column density of NH_3 is derived with the following equation;

$$N_{\text{TOT}}(\text{NH}_3) = \frac{N(J,K)}{g_J \cdot g_I \cdot g_K} Q_{\text{rot}} \exp\left(\frac{E_u(J,K)}{kT_{\text{rot}}}\right) \quad (5)$$

$$\sim N(1,1) \left[\frac{1}{3} \exp\left(\frac{23.3}{T_{\text{rot}}}\right) + 1 + \frac{5}{3} \exp\left(\frac{-41.1}{T_{\text{rot}}}\right) + \frac{14}{3} \exp\left(\frac{-100.2}{T_{\text{rot}}}\right) \right], \quad (6)$$

where Q_{rot} is the partition function as follows:

$$Q_{\text{rot}} = \sum_J \sum_K g_J \cdot g_I \cdot g_K \exp\left(-\frac{E_u(J,K)}{kT_{\text{rot}}}\right) \quad (7)$$

and in which k is the Boltzmann constant, $E_u(J,K)$ is the energy of the inversion transitions above the ground level, g_J is rotational degeneracy, g_I is nuclear spin degeneracy, and g_K is K-degeneracy. Furthermore, we use $E_u(1,1)/k = 23.3$, $E_u(2,2)/k = 64.4$, and $E_u(3,3)/k = 123.5$ taken from the JPL spectral line catalog³ of Pickett et al. (1998).

Figure 6(b) shows a map of the total column density derived at each observed point. The column density is $2 \times 10^{15} \text{ cm}^{-2}$ at the northern region near S255 N in the NH_3 dense clump while the southern region has a lower column density of $< 1 \times 10^{15} \text{ cm}^{-2}$. Assuming a H_2 conversion factor of $X(\text{NH}_3) = 3.0 \times 10^{-8}$ for the Gemini OB1 (Dunham et al. 2010), the column densities of molecular hydrogen in the northern and southern regions were estimated to be $N(\text{H}_2) \sim 7 \times 10^{22}$ and $3 \times 10^{22} \text{ cm}^{-2}$, respectively. These values of H_2 column density are within the same order of magnitude as the $\sim 4 \times 10^{22} \text{ cm}^{-2}$ estimated from CO and 160-500 μm Herschel data (Ladeyschikov et al. 2021).

Finally, we estimated the LTE mass from the H_2 column density at each map point ($N_i(\text{H}_2)$), using the following equation:

³ <https://spec.jpl.nasa.gov>

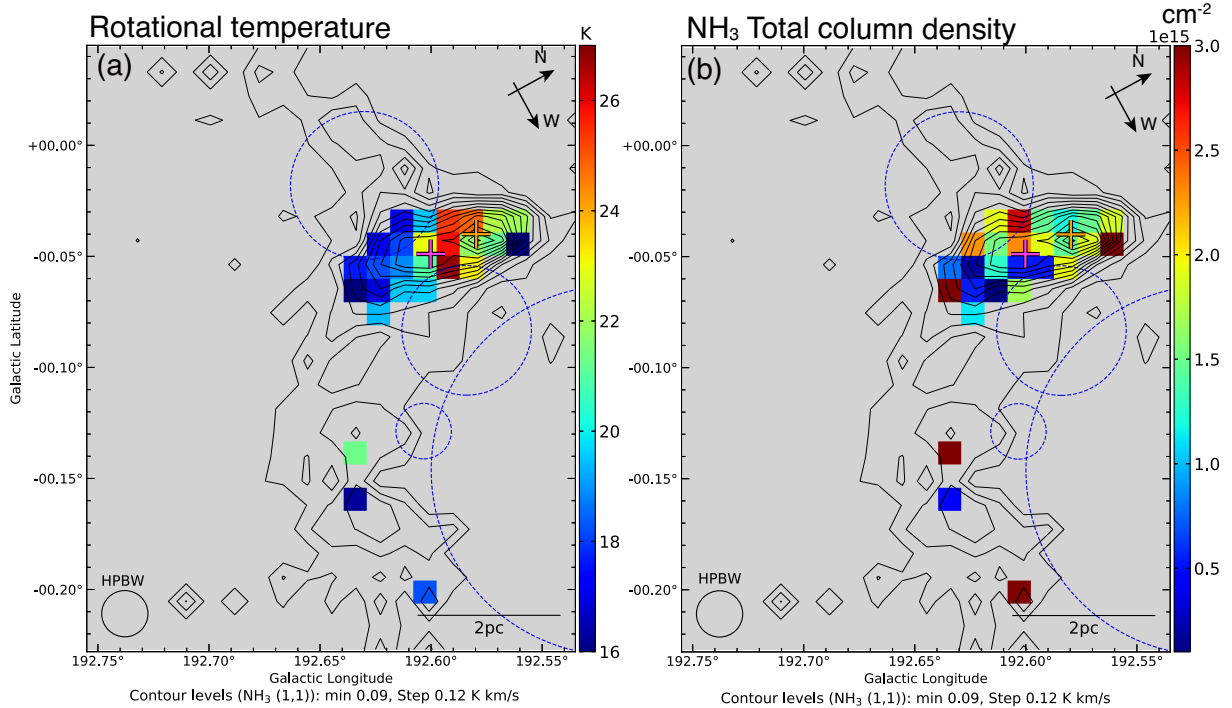


Fig. 6. (a) The rotational temperature map obtained by the (2,2)/(1,1) peak intensity ratio above the 4σ noise level. (b) The NH_3 total column density map above the 4σ noise level. The contours show the NH_3 (J, K) = (1, 1) integrated intensity. The purple, yellow crosses, and blue dotted circles are also the same as Figure 1(b).

$$M_{\text{LTE}} = \mu_{\text{H}_2} m_{\text{H}} D^2 \sum_i \Omega N_i(\text{H}_2), \quad (8)$$

where $\mu_{\text{H}_2} \sim 2.8$ is the mean molecular weight contribution of Helium (e.g., Appendix A.1. of Kauffmann et al. 2008), $m_{\text{H}} = 1.67 \times 10^{-24}$ g is the proton mass, $D = 1.78$ kpc is the distance to S255 IR, and Ω is the solid angle. We obtained $4.9 \times 10^3 M_{\odot}$ for the LTE mass which is consistent within an order of magnitude to the value of $\sim 2.6 \times 10^3 M_{\odot}$ obtained for the CO data (Ladeyschikov et al. 2021).

4 Discussion

4.1 Triggered star formation in S255 IR and S255 N dense molecular clumps

Figure 7 shows the NH_3 (1,1) integrated intensity superposed on the WISE infrared image. The NH_3 intensity peaks coincide with the infrared peaks of S255 IR and S255 N which have total luminosities of $5 \times 10^4 L_{\odot}$ and $1 \times 10^5 L_{\odot}$, respectively (Minier et al. 2005). While Wang et al. (2011) pointed out that S255 N is younger than S255 IR, its luminosity is 2 times greater than that of S255 IR. We also report that the peak of the NH_3 integrated intensity emission is located at S255 N (see Figure 3a). S255 N resides in a reservoir of dense gas and houses active star formation (e.g., Cyganowski et al.

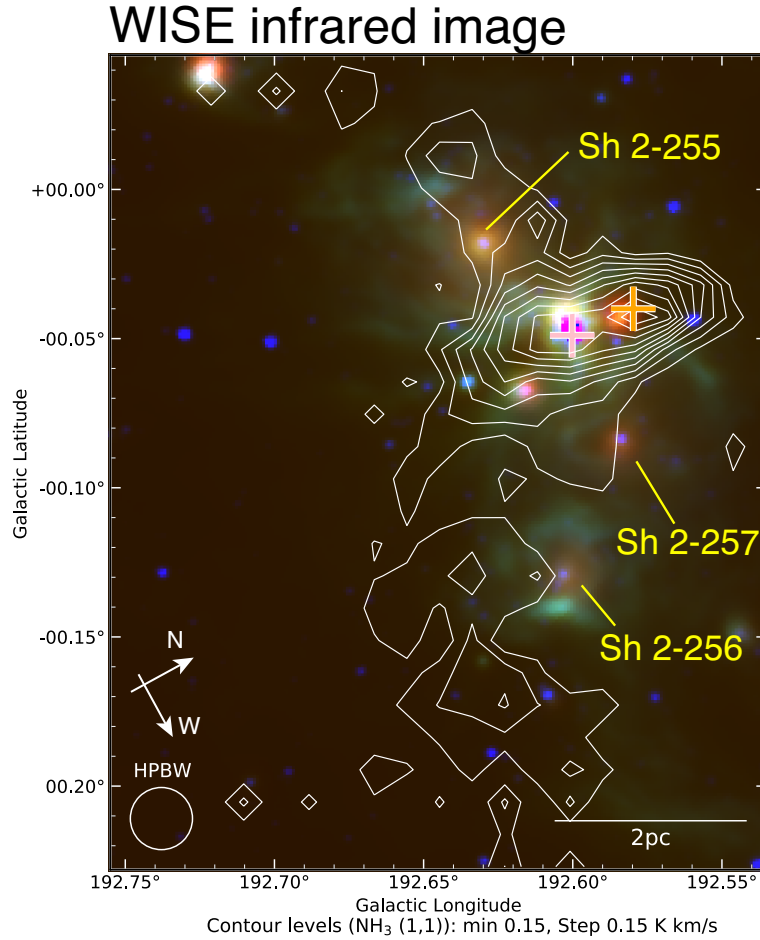


Fig. 7. NH_3 (J, K) = (1, 1) distributions integrated with the velocity range from 4.3 to 11.3 km s^{-1} (white contours) superposed on the three color composite infrared image obtained by the WISE satellite. Blue, green, and red indicate 3.6 μm , 12 μm and 22 μm , respectively. The purple and yellow crosses are also the same as Figure 1(b).

2007; Zemlyanukha et al. 2018), which can be expected to produce further generations of new stars.

Figure 8 shows contours of the NH_3 (1,1) integrated intensity superposed on the ^{12}CO $J=2-1$ integrated intensity map obtained by Bieging et al. (2009). Orange circles represent Class I YSOs, while the white circles indicate Class II YSOs identified by Chavarría et al. (2008). The Class I and Class II YSOs are distributed between Sh 2-255 and Sh 2-257 H II regions concentrated around S255 IR and S255 N, respectively. Following Heiderman & Evans (2015), the time scales of the formation of the Class I and Class II YSOs are ~ 0.5 Myr and ~ 2 Myr, respectively. We therefore infer that S255 IR is in an early stage of star formation based on its concentration of Class I YSOs, identified by Chavarría et al. (2008).

Our observational results also showed large line widths and high rotational temperatures around S255 N and S255 IR (Figure 5b and 6a). We suggest that these NH_3 dense clumps are heated and experience enhanced turbulent motion locally as a result of feedback from the embed-

ded YSO clusters in S255 N and S255 IR. These embedded clusters are likely to be sites of second generation star formation based on their proximity to Sh 2-255 and Sh 2-257. In the case that NH_3 dense clumps are heated by H II regions directly, the rotational temperatures should be enhanced along the H II region boundary uniformly because the temperature of ionized gas has $\sim 10^4$ K (e.g., Draine 2011). However, the NH_3 gas indicates a low rotational temperature (< 18 K) around $(l, b) \sim (192.62, -0.05)$ adjacent to Sh 2-255 (see Figure 6a). This result implies that the NH_3 dense clump might not be affected by shock compression due to the expansion of the Sh 2-255 H II region. Previous NH_3 mapping observations of other massive star-forming regions reported a similar tendency. For example, in the Monkey Head nebula, Chibueze et al. (2013) reported that large line widths and high kinetic temperatures derived by NH_3 observations are localized around embedded compact H II regions. The authors argued that the dense molecular cloud did not form by the expanding H II region in the Monkey Head nebula.

If the Sh 2-255 H II region is expanding and pushing against the molecular cloud, we would expect to see an arc-like morphology of molecular gas, but such a formation is not seen around Sh 2-255 (Figure 8). Indeed, Ojha et al. (2011) pointed out that the collect and collapse process involving H II regions might not be effective in the dense clump between Sh 2-255 and Sh 2-257. While the distributions of line width and rotational temperature enhancements of NH_3 gas investigated in this work positionally correlate with the locations of S255 IR and S255 N, our observations of the dense gas traced by NH_3 do not exhibit clear evidence of interaction from the Sh 2-255 H II region. Consequently, while interaction from Sh 2-255 cannot be ruled out completely, we suggest that other sources of star formation initiation should be considered.

4.2 Impact of the older Sh 2-254 H II region

Finally, we discuss the effect of the older H II region Sh 2-254 which coincides with a hole in the CO emission in this region (see Figure 8). Bieging et al. (2009) proposed that molecular gas around Sh 2-254 was ionized by ultraviolet radiation from its exciting star, or swept up by the expanding H II region. We argue that these effects driven by Sh 2-254 are likely responsible for the induced star formation activity around the western NH_3 peak. The region of western NH_3 emission adjacent to Sh 2-254 and Sh 2-256 also contains Class II objects. Therefore, low-mass star formation has progressed for at least ~ 2 Myr. This time scale is an order magnitude older than the age of Sh 2-256 (0.2 Myr, Chavarría et al. 2008). These Class II low-mass stars were likely to have been formed before triggering by expanding the Sh 2-256 H II region could have occurred. Consequently, we suggest that the star formation around the western NH_3 might have been caused by the older H II region Sh 2-254.

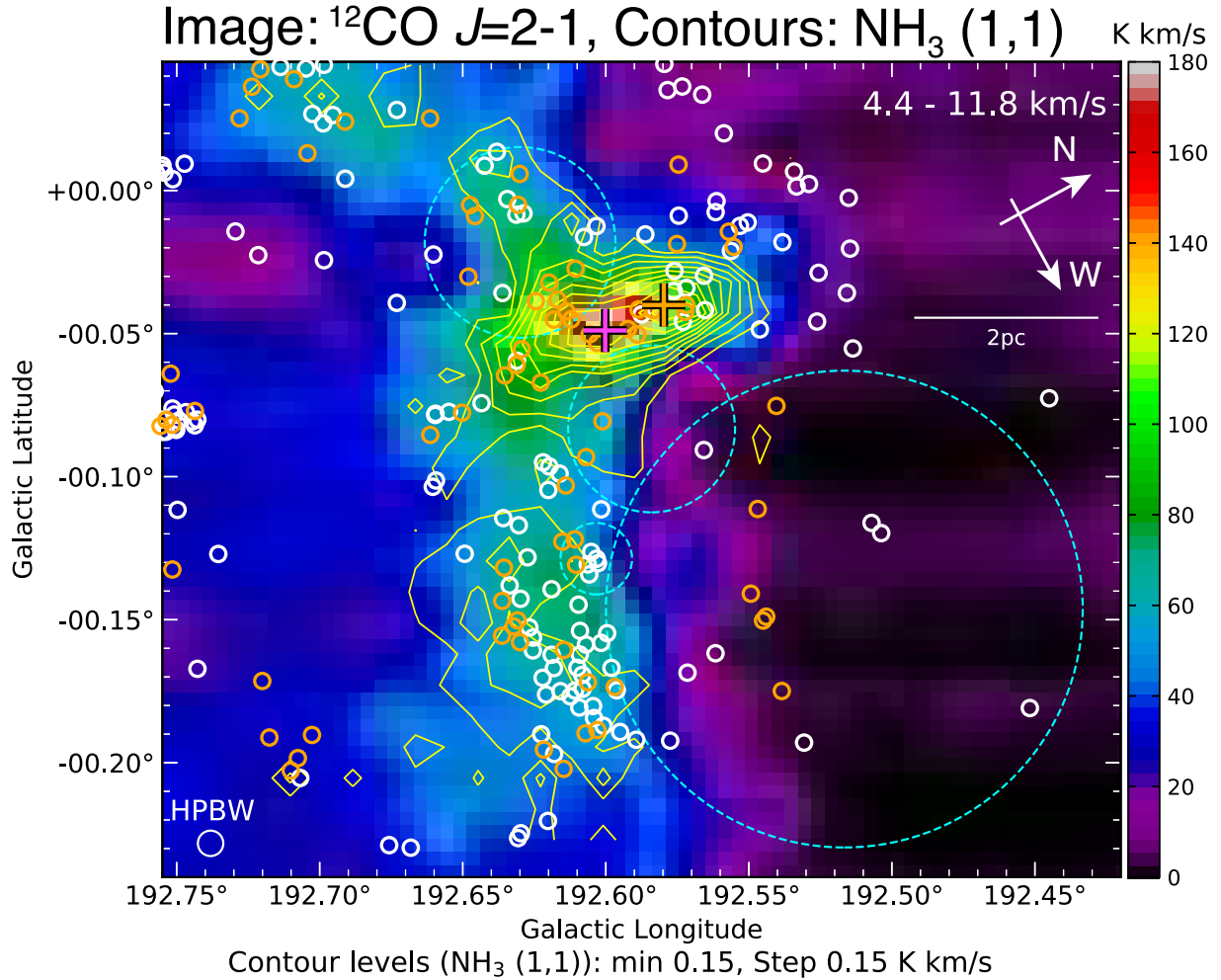


Fig. 8. $\text{NH}_3 (J, K) = (1, 1)$ distributions integrated with the velocity range from 4.3 to 11.3 km s^{-1} (yellow contours) superposed on the $^{12}\text{CO } J=2-1$ integrated intensity map with the velocity range from 4.4 to 11.8 km s^{-1} (Bieging et al. 2009). Orange and white circles indicate Class I, Class II objects identified by Chavarría et al. (2008). The purple, yellow crosses, and blue dotted circles are also the same as Figure 1(b).

The collect and collapse process driven by Sh 2-254 is likely to be responsible for the formation of high-mass protostars (including the exciting sources of Sh 2-256 and Sh 2-257 H II regions) and low-/intermediate mass stars, particularly the YSOs distributed in the western region of the dense molecular cloud. This scenario was suggested previously by Bieging et al. (2009), and our results support their hypothesis of triggered star formation in this region.

5 Summary

The conclusions of this paper are summarized as follows:

1. We carried out $\text{NH}_3 (J, K) = (1, 1), (2, 2),$ and $(3, 3)$ mapping observations toward the Galactic massive star-forming region around Sh 2-255 and Sh 2-257 using the Nobeyama 45-m telescope

as a part of the KAGONMA (KAgoshima Galactic Object survey with the Nobeyama 45-metre telescope by Mapping in Ammonia lines) project.

2. NH_3 (1,1) gas has a size of $3 \text{ pc} \times 2 \text{ pc}$ ($l \times b$), an intensity peak at S255 N, and is located between Sh 2-255 and Sh 2-257.
3. The kinetic temperature derived from the $\text{NH}_3(2,2)/(1,1)$ ratio is $\sim 35 \text{ K}$ near the massive clusters S255 IR. S255 IR and S255 N exhibit large line widths of $\sim 3\text{-}4 \text{ km s}^{-1}$. We suggest that NH_3 gas is affected by stellar feedback from the embedded YSO clusters in S255 IR and S255 N.
4. While the distributions of line width and rotational temperature enhancements of NH_3 gas investigated in this work positionally correlate with the locations of S255 IR and S255 N, our observations of the dense gas traced by NH_3 do not exhibit clear evidence of interaction from the Sh 2-255 H II region.
5. We also detected the NH_3 (1,1) emission at a western region adjacent to the H II regions Sh 2-254 and Sh 2-256. This western region has several Class II YSOs with inferred ages of $\sim 2 \text{ Myr}$, thus are older than Sh 2-256. We conclude that the formation of YSOs at the west side were probably caused by expansion of the older H II region Sh 2-254.

Acknowledgements

The authors are grateful to the anonymous referee for their thoughtful comments on the paper. The Nobeyama 45-m radio telescope is operated by Nobeyama Radio Observatory, a branch of the National Astronomical Observatory of Japan.

The NH_3 back-up observations are promoted on a lot of contributions of Kagoshima university, so the authors would like to thank all them, Dr. Tatsuya Kamezaki, Dr. Gabor Orosz, Dr. Mitsuhiro Matsuo, Mr. Hideo Hamabata, Mr. Tatsuya Baba, Mr. Ikko Hoshihara, and Mr. Masahiro Uesugi. The authors wish to thank all staff of the Nobeyama radio observatory for helpful backup observations. We are grateful to Mr. Shun Saeki of Nagoya University for a useful discussion. The Heinrich Hertz Telescope is operated by the Arizona Radio Observatory, a part of Steward Observatory at The University of Arizona. The Digitized Sky Survey was produced at the Space Telescope Science Institute under U.S. Government grant NAG W-2166. The images of these surveys are based on photographic data obtained using the Oschin Schmidt Telescope on Palomar Mountain and the UK Schmidt Telescope. The plates were processed into the present compressed digital form with the permission of these institutions.

We acknowledge the use of NASA's SkyView facility (<http://skyview.gsfc.nasa.gov>) located at NASA Goddard Space Flight Center.

Software: We used the Astropy, which is the Python package for astronomy (Astropy Collaboration et al. 2013; Astropy Collaboration et al. 2018), NumPy (van der Walt et al. 2011), Matplotlib (Hunter 2007), IPython (Perez, & Granger 2007), Miriad (Sault et al. 1995), and APLpy (Robitaille & Bressert 2012)

References

- Astropy Collaboration, Robitaille, T. P., Tollerud, E. J., et al. 2013, *A&A*, 558, A33
- Astropy Collaboration, Price-Whelan, A. M., Sipőcz, B. M., et al. 2018, *AJ*, 156, 123
- Biegging, J. H., Peters, W. L., Vila Vilaro, B., et al. 2009, *AJ*, 138, 975. doi:10.1088/0004-6256/138/3/975
- Billington, S. J., Urquhart, J. S., Figura, C., et al. 2019, *MNRAS*, 483, 3146. doi:10.1093/mnras/sty3053
- Burns, R. A., Handa, T., Nagayama, T., et al. 2016, *MNRAS*, 460, 283. doi:10.1093/mnras/stw958
- Burns, R. A., Handa, T., Omodaka, T., et al. 2019, *PASJ*, 71, 91. doi:10.1093/pasj/psz074
- Buslaeva, A. I., Kirsanova, M. S., & Punanova, A. F. 2021, *Astronomy Reports*, 65, 488. doi:10.1134/S1063772921060020
- Caratti o Garatti, A., Stecklum, B., Garcia Lopez, R., et al. 2017, *Nature Physics*, 13, 276. doi:10.1038/nphys3942
- Carpenter, J. M., Snell, R. L., & Schloerb, F. P. 1995a, *ApJ*, 445, 246. doi:10.1086/175692
- Carpenter, J. M., Snell, R. L., & Schloerb, F. P. 1995b, *ApJ*, 450, 201. doi:10.1086/176132
- Cesaroni, R., Moscadelli, L., Neri, R., et al. 2018, *A&A*, 612, A103. doi:10.1051/0004-6361/201732238
- Chavarría, L. A., Allen, L. E., Hora, J. L., et al. 2008, *ApJ*, 682, 445. doi:10.1086/588810
- Chavarría, L., Allen, L., Brunt, C., et al. 2014, *MNRAS*, 439, 3719. doi:10.1093/mnras/stu224
- Chibueze, J. O., Imura, K., Omodaka, T., et al. 2013, *ApJ*, 762, 17. doi:10.1088/0004-637X/762/1/17
- Chopinnet, M., Deharveng-Baudel, L., & Lortet-Zuckermann, M. C. 1974, *A&A*, 30, 233
- Cyganowski, C. J., Brogan, C. L., & Hunter, T. R. 2007, *AJ*, 134, 346. doi:10.1086/518740
- Dunham, M. K., Rosolowsky, E., Evans, N. J., et al. 2010, *ApJ*, 717, 1157. doi:10.1088/0004-637X/717/2/1157
- Draine, B. T. 2011, *Physics of the Interstellar and Intergalactic Medium* by Bruce T. Draine. Princeton University Press, 2011. ISBN: 978-0-691-12214-4
- Evans, N. J., Blair, G. N., & Beckwith, S. 1977, *ApJ*, 217, 448. doi:10.1086/155594
- Fujisawa, K., Yonekura, Y., Sugiyama, K., et al. 2015, *The Astronomer's Telegram*, 8286
- Heiderman, A. & Evans, N. J. 2015, *ApJ*, 806, 231. doi:10.1088/0004-637X/806/2/231
- Heyer, M. H., Snell, R. L., Morgan, J., et al. 1989, *ApJ*, 346, 220. doi:10.1086/168003
- Hirata, Y., Handa, T., Murase, T., et al. 2022, in preparation.
- Hirota, T., Cesaroni, R., Moscadelli, L., et al. 2021, *A&A*, 647, A23. doi:10.1051/0004-6361/202039798

Howard, E. M., Pipher, J. L., & Forrest, W. J. 1997, *ApJ*, 481, 327. doi:10.1086/304046

Ho, P. T. P. & Townes, C. H. 1983, *ARA&A*, 21, 239. doi:10.1146/annurev.aa.21.090183.001323

Hunter, J. D. 2007, *Computing in Science and Engineering*, 9, 90

Ikedda, M., Nishiyama, K., Ohishi, M., et al. 2001, *Astronomical Data Analysis Software and Systems X*, 238, 522

Itoh, Y., Tamura, M., Suto, H., et al. 2001, *PASJ*, 53, 495. doi:10.1093/pasj/53.3.495

Kamazaki, T., Okumura, S. K., Chikada, Y., et al. 2012, *PASJ*, 64, 29

Kauffmann, J., Bertoldi, F., Bourke, T. L., et al. 2008, *A&A*, 487, 993. doi:10.1051/0004-6361:200809481

Kawamura, A., Onishi, T., Yonekura, Y., et al. 1998, *ApJS*, 117, 387. doi:10.1086/313119

Kuno, N., et al. 2011, in *Proc. 2011 XXXth URSI General Assembly and Scientific Symposium (New York: IEEE)*, 3670⁴

Kutner, M. L., & Ulich, B. L. 1981, *ApJ*, 250, 341

Ladeyschikov, D. A., Kirsanova, M. S., Sobolev, A. M., et al. 2021, *MNRAS*, 506, 4447. doi:10.1093/mnras/stab1821

Lim, B., Sung, H., Hur, H., et al. 2015, *Journal of Korean Astronomical Society*, 48, 343. doi:10.5303/JKAS.2015.48.6.343

Liu, S.-Y., Su, Y.-N., Zinchenko, I., et al. 2018, *ApJL*, 863, L12. doi:10.3847/2041-8213/aad63a

Liu, S.-Y., Su, Y.-N., Zinchenko, I., et al. 2020, *ApJ*, 904, 181. doi:10.3847/1538-4357/abc0ec

Mangum, J. G., Wootten, A., & Mundy, L. G. 1992, *ApJ*, 388, 467. doi:10.1086/171167

Mangum, J. G. & Shirley, Y. L. 2015, *PASP*, 127, 266. doi:10.1086/680323

McGary, R. S. & Ho, P. T. P. 2002, *ApJ*, 577, 757. doi:10.1086/342233

McGlynn, T., Scollick, K., & White, N. 1998, *New Horizons from Multi-Wavelength Sky Surveys*, 179, 465

Minier, V., Burton, M. G., Hill, T., et al. 2005, *A&A*, 429, 945. doi:10.1051/0004-6361:20041137

Miralles, M. P., Salas, L., Cruz-González, I., et al. 1997, *ApJ*, 488, 749. doi:10.1086/304713

Mizuno, S. 1982, *Ap&SS*, 87, 121. doi:10.1007/BF00648913

Murase, T., Handa, T., Maebata, M., et al. 2020, *Origins: From the Protosun to the First Steps of Life*, 345, 353. doi:10.1017/S174392131900200X

Murase, T., Handa, T., Hirata, Y., et al. 2022, *MNRAS*, 510, 1106

Nagayama, T., Omodaka, T., Handa, T., et al. 2007, *PASJ*, 59, 869. doi:10.1093/pasj/59.5.869

Nagayama, T., Omodaka, T., Handa, T., et al. 2009, *PASJ*, 61, 1023. doi:10.1093/pasj/61.5.1023

Nakano, M., Kogure, T., Mizuno, S., et al. 1983, *Ap&SS*, 89, 407. doi:10.1007/BF00655994

Nakano, M., Soejima, T., Chibueze, J. O., et al. 2017, *PASJ*, 69, 16. doi:10.1093/pasj/psw120

⁴ <http://ieeexplore.ieee.org/xpl/articleDetails.jsp?arnumber=6051296>

Ojha, D. K., Samal, M. R., Pandey, A. K., et al. 2011, *ApJ*, 738, 156. doi:10.1088/0004-637X/738/2/156

Omodaka, T., Morimoto, M., Kawaguchi, N., et al. 1994, *VLBI TechnologyY: Progress and Future Observational Possibilities*, 191

Perez, F., & Granger, B. E. 2007, *Computing in Science and Engineering*, 9, 21

Pickett, H. M., Poynter, R. L., Cohen, E. A., et al. 1998, *J. Quant. Spectrosc. Radiat. Transfer*, 60, 883. doi:10.1016/S0022-4073(98)00091-0

Pipher, J. L. & Soifer, B. T. 1976, *A&A*, 46, 153

Robitaille, T., & Bressert, E. 2012, *APLpy: Astronomical Plotting Library in Python*, ascl:1208.017

Rygl, K. L. J., Brunthaler, A., Reid, M. J., et al. 2010, *A&A*, 511, A2. doi:10.1051/0004-6361/200913135

Samal, M. R., Ojha, D. K., Jose, J., et al. 2015, *A&A*, 581, A5. doi:10.1051/0004-6361/201322787

Sault, R. J., Teuben, P. J., & Wright, M. C. H. 1995, *Astronomical Data Analysis Software and Systems IV*, 77, 433

Sharpless, S. 1959, *ApJS*, 4, 257

Szymczak, M., Olech, M., Wolak, P., et al. 2018, *A&A*, 617, A80. doi:10.1051/0004-6361/201833443

Tafalla, M., Myers, P. C., Caselli, P., et al. 2004, *A&A*, 416, 191. doi:10.1051/0004-6361:20031704

Toujima, H., Nagayama, T., Omodaka, T., et al. 2011, *PASJ*, 63, 1259. doi:10.1093/pasj/63.6.1259

Turner, B. E. 1991, *ApJS*, 76, 617. doi:10.1086/191577

Uchiyama, M., Yamashita, T., Sugiyama, K., et al. 2020, *PASJ*, 72, 4. doi:10.1093/pasj/psz122

Ulich, B. L., & Haas, R. W. 1976, *ApJS*, 30, 247

Urquhart, J. S., Morgan, L. K., Figura, C. C., et al. 2011, *MNRAS*, 418, 1689. doi:10.1111/j.1365-2966.2011.19594.x

van der Walt, S., Colbert, S. C., & Varoquaux, G. 2011, *Computing in Science and Engineering*, 13, 22

Wang, Y., Beuther, H., Bik, A., et al. 2011, *A&A*, 527, A32. doi:10.1051/0004-6361/201015543

Wang, C., Yang, J., Xu, Y., et al. 2017, *ApJS*, 230, 5. doi:10.3847/1538-4365/aa6c6b

Wienen, M., Wyrowski, F., Menten, K. M., et al. 2018, *A&A*, 609, A125. doi:10.1051/0004-6361/201526384

Wilson, T. L., Rohlfs, K., & Hüttemeister, S. 2013, *Tools of Radio Astronomy; Astronomy and Astrophysics Library*. ISBN 978-3-642-39949-7. Springer-Verlag Berlin Heidelberg

Wright, E. L., Eisenhardt, P. R. M., Mainzer, A. K., et al. 2010, *AJ*, 140, 1868. doi:10.1088/0004-6256/140/6/1868

Zemlyanukha, P. M., Zinchenko, I. I., Sali, S. V., et al. 2018, *Astronomy Reports*, 62, 326. doi:10.1134/S1063772918050074

Zinchenko, I., Henning, T., & Schreyer, K. 1997, *A&AS*, 124, 385. doi:10.1051/aas:1997361

Zinchenko, I., Caselli, P., & Pirogov, L. 2009, *MNRAS*, 395, 2234. doi:10.1111/j.1365-2966.2009.14687.x

Zinchenko, I., Liu, S.-Y., Su, Y.-N., et al. 2012, *ApJ*, 755, 177. doi:10.1088/0004-637X/755/2/177

Zinchenko, I., Liu, S.-Y., Su, Y.-N., et al. 2015, ApJ, 810, 10. doi:10.1088/0004-637X/810/1/10

Zinchenko, I. I., Liu, S.-Y., Su, Y.-N., et al. 2020, ApJ, 889, 43. doi:10.3847/1538-4357/ab5c18

Zucker, C., Speagle, J. S., Schlafly, E. F., et al. 2019, ApJ, 879, 125. doi:10.3847/1538-4357/ab2388